

Single-Step-Lithography Micro-Stepper Based on Frictional Contact and Chiral Metamaterial

Xiaojun Tan, Julio Andrés Iglesias Martínez, Gwenn Ulliac, Bing Wang,* Linzhi Wu, Johnny Moughames, Marina Raschetti, Vincent Laude, and Muamer Kadic*

Stepper motors and actuators are among the main constituents of control motion devices. They are complex multibody systems with rather large overall volume due to their multifunctional parts and elaborate technological assembly processes. Miniaturization of individual parts is still posing assembly problems. In this paper, a single-step lithography process to fabricate a micro-stepper engine with an accurate micrometric rotation axis and an overall sub-millimeter size is demonstrated. The device is based on the frictional contacts and chiral metamaterials to get rid of the dependence on the accuracy of parts. The functional aspects of fabricated samples are discussed for many rotation cycles and for different frictional surfaces.

1. Introduction

Contact-based mechanics has played a crucial rule for the last centuries, from steam engines^[1] to precision mechanics,^[2–4] in particular in the watchmaking industry.^[5] At the macro-scale, actuation mechanisms and the resulting precision have been improving for decades; it is now rather usual to request at least micrometric precision for macroscopic (say, centimetric) parts. A car engine is a nice example of that. When a car clutch^[6,7] is activated, decoupling results between a rotatory part and another rotation-based mechanism. Even at this scale, a particular technological trick is used to avoid misalignment between the two mechanisms and a low-sensitivity mechanism based on friction-like contact^[8,9] is crucial. When it comes to small size mechanisms, it is very complex to obtain and assemble such systems because the precision must scale accordingly.

X. Tan, J. A. I. Martínez, G. Ulliac, J. Moughames, M. Raschetti, V. Laude, M. Kadic

Institut FEMTO-ST
CNRS UMR 6174
University Bourgogne Franche-Comté
Besançon 25000, France
E-mail: muamer.kadic@femto-st.fr

X. Tan, B. Wang, L. Wu
National Key Laboratory of Science and Technology on Advanced Composites in Special Environments
Harbin Institute of Technology
Harbin 150001, P. R. China
E-mail: wangbing86@hit.edu.cn

 The ORCID identification number(s) for the author(s) of this article can be found under <https://doi.org/10.1002/smll.202202128>.

DOI: 10.1002/smll.202202128

At the micro and nanoscale, attempts at complex mechanical systems can be roughly divided into two technical paths. One is chemical or biological robots^[10–12] that do not have obvious traditional mechanical structure equivalents. Through physical field or self driving, certain specific functions such as conveying cargo^[13,14] can be realized. Another path is to achieve miniaturization of complex mechanical systems through advanced manufacturing and micro assembly technology. For example, microscale mechanical actuators were printed at the microscale thanks to two-

photon photo-polymerization.^[15–17] Some authors^[18,19] further tried to assemble simple microscale parts, such as micro-parts with dovetails and gears. However, at present, it remains almost impossible to achieve complex structures with multiple parts such as mechanical engines at the microscale because it is hard to meet the accuracy of parts.

During the last decade, 3D printing technology has experienced an exponential growth,^[20–22] from simple Stereo lithography Appearanceor Selective Laser Sintering^[23] to advanced 3D Direct Laser Writing (DLW) that enables sub-micron printing precision in three dimensions.^[24–28] Even if extremely small parts can be achieved accurately, their relative precision is in contrast rather poor. As a simple comparison, micrometric precision is common for the mechanical parts of engines of an overall size about tens of centimeters, resulting in an accuracy ratio of the order of 1/10000 (10^{-4}). In order to achieve similar precision for a micrometric object whose size is in the order of 10 μm , we would need nanometric accuracy. This is simply not possible with current 3D additive fabrication processes. An alternative way must thus be conceived to design and actuate multibody dynamical parts and to use them as functional devices.

The development of metamaterials^[29–36] has drifted from simple effective material properties to complex mechanical functional systems at the microscale. Mechanical metamaterials can indeed replace certain precision parts in complex mechanical systems. For example, mechanical metamaterials were used to implement spatially textured functionalities.^[37] Auxetic metamaterials^[30,38] are also widely used in the field of medical devices.^[39] Self-guided shape-changing metamaterials^[40–44] are expected to replace folding machinery and telescopic mechanisms, and bistable structures to replace traditional propellers and drive bionic fish.^[45] Buckling-driven

materials can act as pick and place end-effectors like manipulators.^[46] In addition, metamaterials are used to replace complex vibration isolation mechanical equipment and to implement related functions.^[33,47,48] Although, the above researches only substitute some complex mechanical systems or parts by using mechanical metamaterials at the macroscale, this substitution effectively reduces the requirements for machining accuracy of key parts, which is particularly critical for the preparation of complex structures at the microscale.

In this paper, we discuss the realization of a micro-stepper with a clutch using a single-step 3D printing process.^[27,45,49–51] The stepper is based on precision-forgiving deformation principles, relies on frictional contacts and uses a twisting mechanical metamaterial.^[51–56] The clutch is combined with a unidirectional pushing mechanism, thus producing a stepping engine with a stepping angle of 75° . We emphasize that here we are interested in obtaining a large stepping angle, rather than a small one, to yield faster rotation operation.

2. Design

In this section, we describe the operating principle of the stepping engine and how each part is designed to reach the overall functionality. The mechanical parts are depicted in **Figure 1**. A chiral elastic column is placed at the top of a moving part (detached mechanically from the rest of the structure) and is placed on a rotation axis. Compression of the external elastic springs (in the form of thin curved plates) causes the chiral elastic column to twist.^[51,57] Since it is in frictional contact with the ratchet, the latter rotates until the stepping angle is reached at which point compression is released. A pawl is used as a blocking mechanism in order to avoid reciprocal motion (a backward-rotation). The thin-curved plates are used as a support and to exert a restoring force during the unloading cycle.

In our design, we have fixed the minimum rotational step by the ratchet's gear to 75° corresponding to 48 teeth. For a proper understanding of the extremely complex geometry, we suggest the reader to carefully consider the full computer aided design (CAD) representation in Figure S1 (Supporting Information) and to watch the overall rotational behavior for many cycles that is provided as a Video in Supporting Information. As can be observed, the complexity of the presented mechanical system is very high. In contrast, most of the previous studies of micro-scale mechanical systems focused on simple structures.

From the strict elastic point of view, the deformation of the chiral elastic column (see Figure 1b) must be reversible, i.e., no plastification must occur and should obviously not destroy the sample. All parts were designed in such a way that the maximum local strain in the sample does not exceed 8%.

In addition, once contact is made, friction should be large enough to transmit the rotational force from the chiral elastic column to the ratchet. In a 3D printing process, it is, in fact, natural and easy to achieve rather rough surfaces, which is taken advantage of in this study. We have particularly paid attention to obtain a frictional coefficient large enough to ensure the right coupling and to get accurate rotation angles. Samples are printed using a Nanoscribe GT micro-lithography setup based on the two-photon absorption principle (see Experimental Section).

Prior to testing, the fabricated structure was observed with a scanning electron microscopy (SEM), as shown in **Figure 2a** with an oblique view. More information about this specific procedure are given in the Experimental Section. Most importantly, all parts can be identified in the CAD file provided in the Supporting Information. A zoom on the crucial pawl, or locking mechanism, is shown in Figure 2b. On the top view of Figure 2c, one can observe the small keyway that is used to monitor rotation during experiments. It is important to note that the part that is the most difficult to print is the gap between the chiral elastic

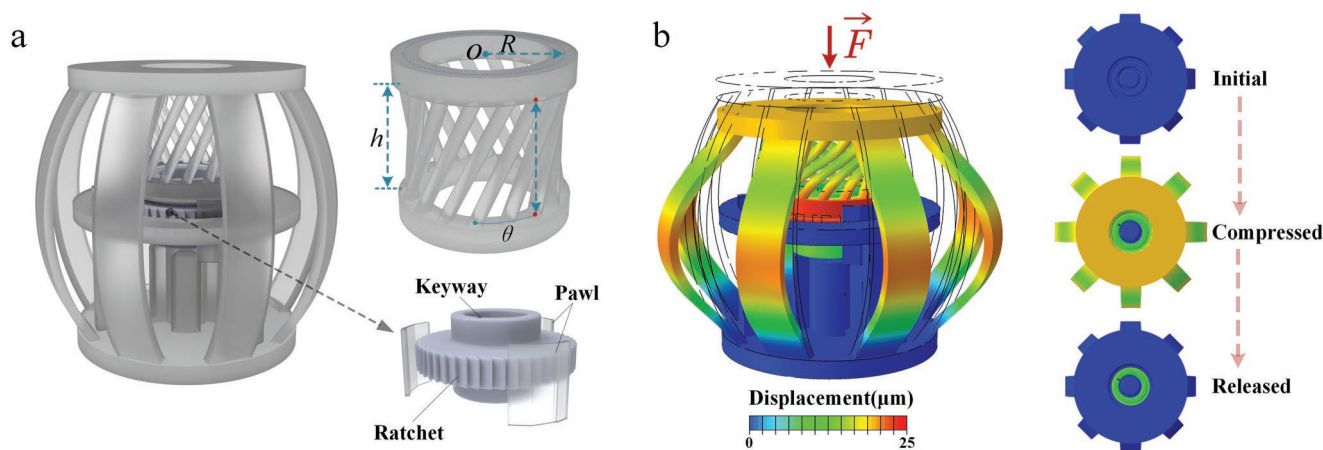


Figure 1. Principle of the micro-stepper. a) An oblique view shows that the stepper contains a chiral elastic column, based on a mechanical metamaterial, that is twisting under a unidirectional compression; the chiral metamaterial part is depicted as a subpanel. The bottom subpanel is a zoom on the central part that shows the ratchet moving under frictional contact with the motionless central plate. A pawl is placed as a blocking mechanism and a keyway is included for rotation monitoring. A full CAD representation of the structure is presented in Figure S1 (Supporting Information). b) Under uniaxial compression, an oblique view and top views are shown of the deformed structure for 3 different pre-deformed states: initial state, compression to the nominal stepping rotation angle, and compression-released case leaving the ratchet in its first stepping angle. Geometrical parameters are the height of the chiral metamaterial part $h = 57.57 \mu\text{m}$, the radius of the chiral metamaterial part $R = 36 \mu\text{m}$, and the angle of the chiral elastic column $\theta = 45^\circ$. The colorbar for total displacement shows which parts are actually moving during operation.

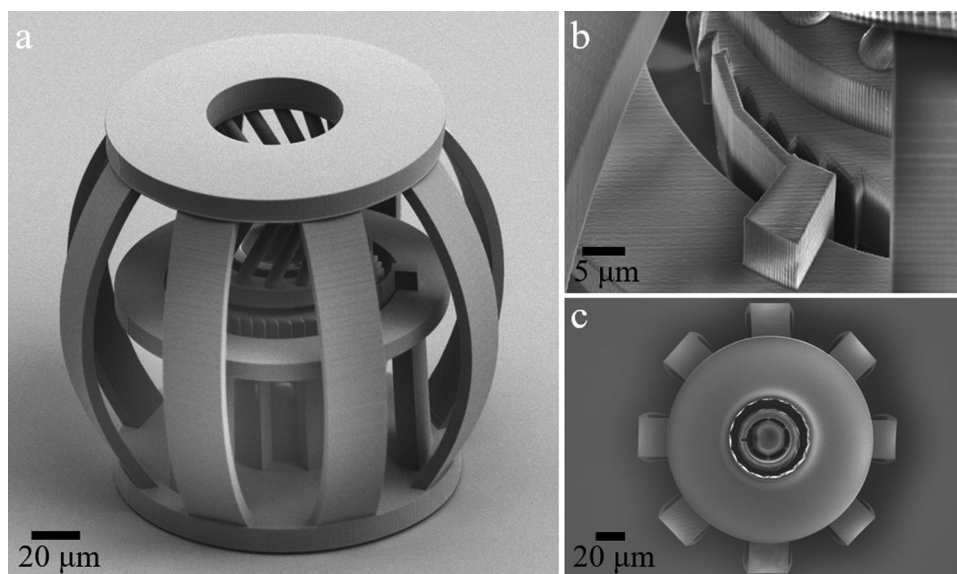


Figure 2. SEM imaging of the fabricated micro-stepper. a) The full micro-stepper is fabricated using the DLW microprinting technique. b) Zoom on the locking mechanism (pawl) that prevents the central plate from moving backward during the unloading phase. c) Top view of the stepper.

column and the ratchet, which is supposed to be on the order of $3\ \mu\text{m}$. During development of the resist, un-polymerized monomer can easily be trapped and remain in this small gap. We could overcome this difficulty by using critical point drying, thus ensuring that the chiral elastic column is not mechanically connected to the ratchet in the rest position of the micro-stepper.

3. Results

Rotational stepping of the samples was characterized using a homemade optical setup (see Experimental Section). Results of the rotational stepping under uniaxial loading are summarized in **Figure 3**. First, we consider the clean polymer sample obtained directly from 3D printing. In **Figure 3a**, the stepping process progresses from left to right, starting from the initial rest state of the stepper and further applying a progressive compression deforming the center of the structure until the final release of the force. Overall, the elastic deformation of the overall structure is reversible in the vertical loading direction (the stepper recovers its initial shape). The compression process is repeated n -th times to increase rotation step by step. Top views of the rotating stepper are shown in **Figure 3b** for steps $n = \{0; 7; 14; 21; 30\}$. In each optical image, the red arrow indicates the real-time position of the keyway. It can clearly be seen that the arrow is constantly rotating. A 2π rotation is obtained in ≈ 30 compression steps.

Second, we consider the same sample but with the addition of a 5-nm-thick sputtered chromium layer, as shown in **Figure 3c**. We emphasize that the structure is the same, though optical images are now extremely distorted and difficult to read as certain parts are optically flat and metallic, and thus strongly reflect the incoming light. However, the most important part for the observation is the keyway that remains clearly visible during rotation. The primary purpose of adding an additional metallic layer is to increase the durability of the stepper, but it

also allows one to control the value of the effective friction coefficient α , defined as the ratio $\alpha = F_s/N$ of the resulting tangential force F_s to the force applied normally to the sliding interface N . In order to quantify the accuracy of printing and material quality, we repeated the displacement-force measurements for many cycles. The results are gathered in **Figures 3d,e**. Good accuracy and repeatability are observed for both sputtered and un-sputtered samples.

In our design procedure, we had to assume an effective friction coefficient. We now discuss how its value can be estimated. **Figure 4a** shows the variation of the induced rotation angle versus the loading vertical displacement. Two sets of measurements were performed for the clean polymer sample and for the chromium sputtered sample. It is understood that in the latter case, the additional metallic layer brings in a sliding mechanism to the contact and can thus decrease friction, or equivalently sticking between surfaces. In order to fit both experimental results, in **Figure 4a**, we adjusted the effective friction coefficient to $\alpha = 0.27$ for the pure polymer sample and to $\alpha = 0.15$ for the sputtered sample. In order to double check the experimental validity of the obtained effective friction coefficient, we further investigated a combination of specifically designed frictional structures (**Figure S3**, Supporting Information) and we derived the value of $\alpha = 0.27 - 0.36$. In the Supporting Information, a totally different design, using frictional contacts and polymer deformation, is used. We should remind the reader that at this scale, it is almost impossible to use the standard macroscopic scale technique to measure the friction coefficient because of force measurements and alignment issues. We overcome this limit by using a structure displaying frictional and deformation effects with the same order of magnitude, thus confirming the right range of friction coefficient obtained for the polymer contacts. To further investigate the influence of geometrical parameters, **Figure 4b** depicts numerical simulation results for samples with varying geometrical parameters. Increasing the chiral angle θ beyond the initial

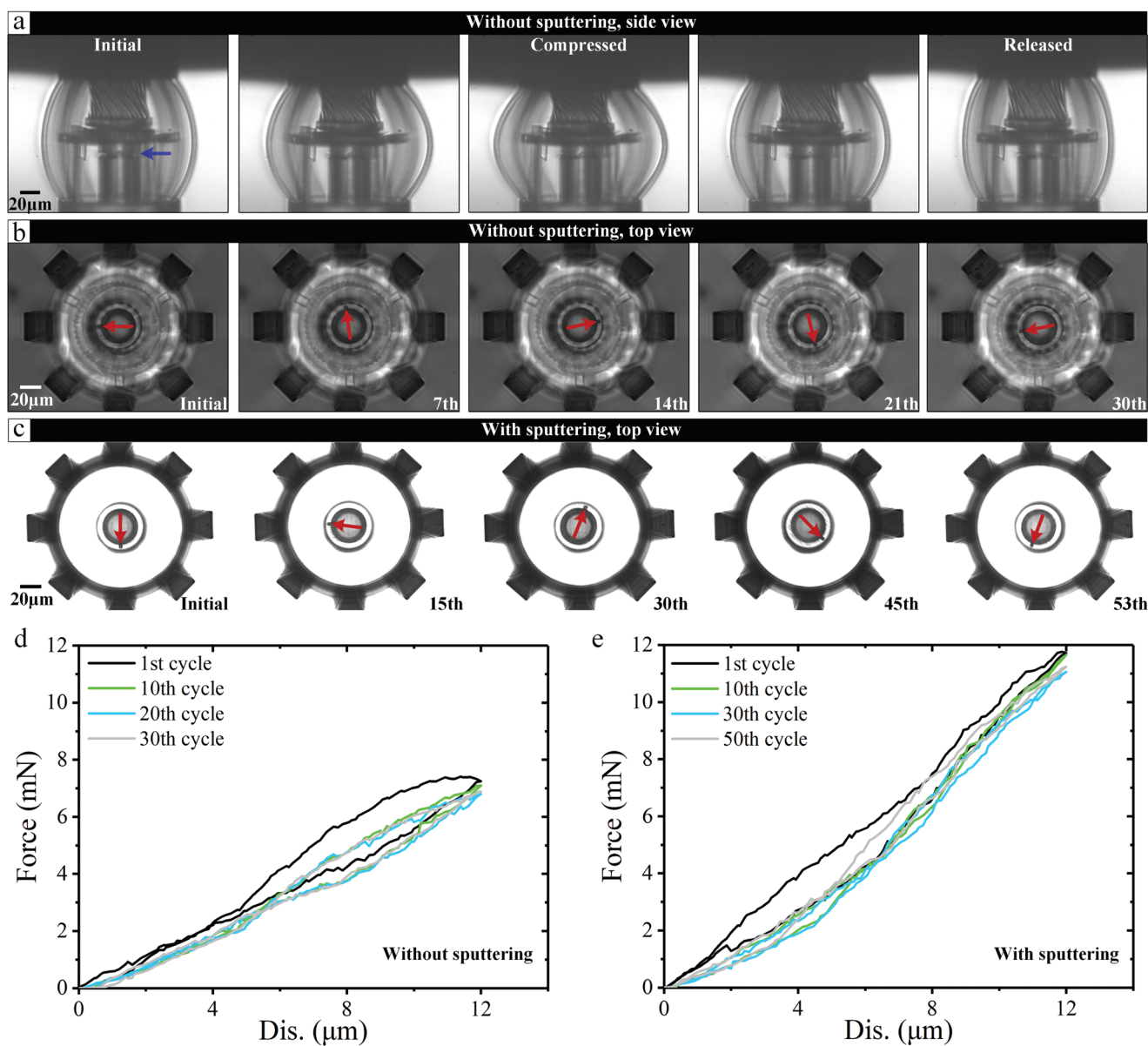


Figure 3. Experimental tests. a) Side optical images of the deformation process from initial via compression to released state. b) Top optical images show the rotation process during multiple actuation of the micro-stepper. A red arrow has been added to indicate the rotation of the ratchet. Images are shown for the $n = \{0, 7, 14, 21, 30\}$ loading cycles for a sample without surface processing. c) Same as (b), but for a chromium sputtered (layer thickness ≈ 5 nm) sample, for cycles $n = \{0, 15, 30, 45, 53\}$. In both panels (b) and (c) the 0th cycle is used as the initial state. Force-displacement (Dis.) curves obtained during cycling are shown for the d) clean polymer sample and for the e) chromium coated sample.

value of 45° has the effect of decreasing the resulting rotation of the ratchet. In contrast, decreasing the radius R appears to have the beneficial effect of increasing the rotation. However, it makes printing more challenging. Increasing h has a similar effect and also improves the compactness of the design. From these results, it can be inferred that the design could be further optimized to produce a larger rotation angle for a given loading displacement. A more comprehensive relationship between the chiral metamaterial part and the rotation angle can be found in the literature.^[52–54] The red line in Figure 4b shows the variation of the rotation angle as a function of the friction coefficient for the initial design.

Finally, we emphasise that the micro-stepper is fabricated in a single step of lithography. In this respect, a single STL file is the only requirement for fabrication and is available as a Supporting Information. Using the provided file, we reprinted the structure several times to observe the repeatability and reproducibility of the results. Although under SEM imaging, all samples look the same; their cycling response might fluctuate. Figure S2 (Supporting Information) reports cycling measurements performed for three different printed samples. A very nice reproducible behavior can be observed. We aim here to attract the reader's attention to the quality of the obtained microstructures.

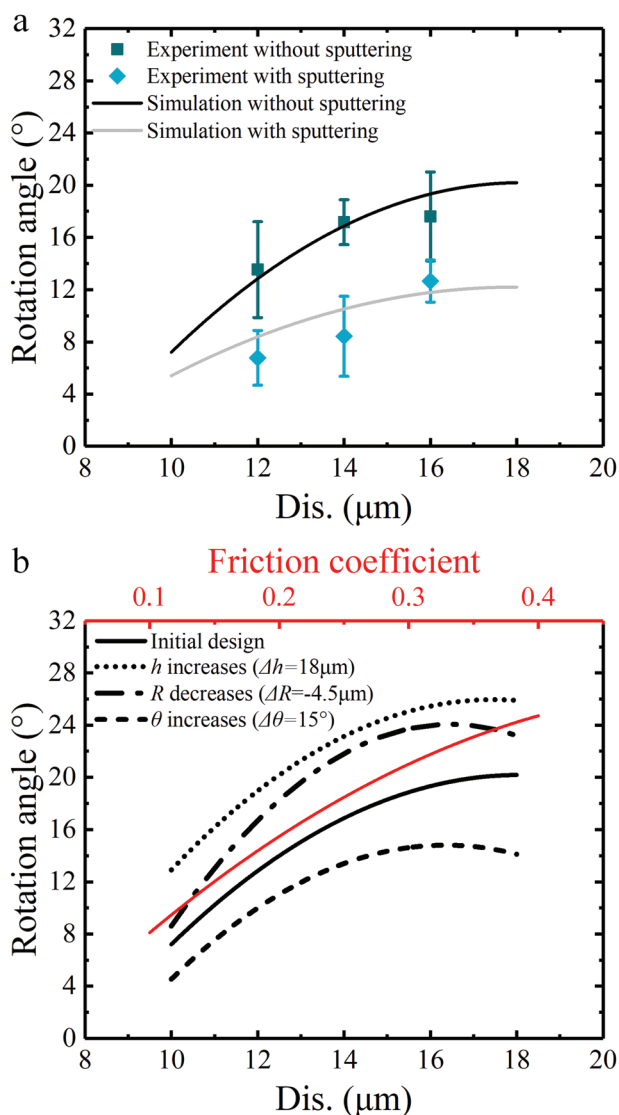


Figure 4. a) Rotation angle for the clean polymer sample and for the chromium sputtered sample versus the displacement (Dis.) amplitude of loading. Points are for experimental measurements and lines are for numerical results. b) Numerical parametric study of the influence of the geometrical parameter (the height of the chiral metamaterial part h , the radius of the chiral metamaterial part R , and the angle of the chiral elastic column θ) and the friction coefficient on the rotation angle. The loading displacement (Dis.) is set to 16 μm in the latter case.

4. Conclusion

In this work, we have shown that using frictional contacts, we can design a single-step lithography process to fabricate a 3D micro-metric stepper. Using unidirectional pushing, combined with a locking mechanism, we used a chiral mechanical metamaterial with a clutch to build a stepper with a stepping angle of 75° by design. Under test, excellent repeatability and cycling was achieved. Furthermore, similar mechanisms can be widely used at microscale to avoid multibody forces and torque transmission problems. The stepper achieved is a promising example for micro-robotic actuation and can potentially

be integrated in a more complex design to provide translational and rotational degrees of freedom.

5. Experimental Section

Fabrication: The micro-scale samples investigated in this work were fabricated by 3D DLW. To this aim, a commercial 3D printer (Photonic Professional GT+, Nanoscribe GmbH) operating based on the two-photon lithography method was used.

The photoresin selected to produce the micro-stepper was the commercial negative tone IP-Dip2 resist (Nanoscribe GmbH) that is customized to work well with the Nanoscribe 3D printer. Other materials, such as hydrogel, composites, and liquid crystal elastomers, could also be applied to expand the applications of the presented device in the future. Furthermore, the slicing and hatching distances were set equal to 0.3 and 0.2 μm , respectively. A drop of Dip2 resist was deposited on a fused silica substrate with dimensions $25 \times 25 \times 0.7 \text{ mm}^3$ and photopolymerized with a femtosecond laser operating at $\lambda = 780 \text{ nm}$ and a 63X objective.

To improve the adhesion properties of the IP-Dip2 resist and so to ensure a better connection of the printed sample with the substrate, fused silica substrates were pre-treated with oxygen plasma (Corial 200R, RIE etch system) for 5 min. A laser power of 60 mW and a Galvanometric scan speed of 10 mm s^{-1} were used for the whole fabrication process. After printing, the sample was developed for 40 min in a hot propylene glycol methyl ether acetate (PGMEA) solution with a magnetic stirrer bar (300 rpm/ 70°) in order to remove all the unexposed photoresist. The sample was further rinsed for 3 min in isopropyl alcohol (IPA) to clear the developer. In order to avoid sticking between some parts of the structures, critical point drying was used (Autosamdri 931, Tousimis). This technique is efficient for drying 3D delicate samples.

SEM Imaging and Chromium Sputtering: The fabricated structures were observed using an ApreoS, ThermoFisher SEM in Optiplan mode. To obtain high quality images, the surface was previously coated with a thin layer of chromium by sputtering (ACE600, Leica). The chromium thickness obtained was less than 5 nm. The imaging voltage was kept low (<10 kV) to avoid damaging the structures. Images were taken at an angle of 62° .

Finite Element Method: Design was performed using the finite element method (FEM) by solving the linear elasticity model combined with frictional contacts. The bottom of the structure was assumed fixed $u = 0$, and it was solved numerically by the following formula:

$$-\nabla \cdot \sigma = F_{\text{ext}} \quad (1)$$

where $\sigma = C : \varepsilon$ is the stress, with the symmetrized strain $\varepsilon = \frac{1}{2}[\nabla u + (\nabla u)^T]$ and F_{ext} being the external loading body forces. The isotropic elastic parameters were used for the polymer, namely Young's modulus $E = 2.89 \text{ GPa}$ and Poisson's coefficient $\nu = 0.4$. In order to take friction into account, an effective friction coefficient α between touching interfaces during compressional tests was introduced. In addition, geometrical nonlinearities during compression via an automated moving mesh refinement procedure managed by the commercial software ABAQUS were considered. A total of 18 cycles were computed and the average rotation angle was selected for display, considering fluctuations in each cycle resulting from structural characteristics. Indeed, as it can be observed in Figure S1 (Supporting Information), there is a small gap between the ratchet and the pawl. Therefore, the ratchet was not exactly on axis, and a slight eccentric movement could occur when under drive, directly leading to a difference in rotation angle between each cycle.

Testing: In order to test the mechanical properties of the analyzed samples, the uniaxial compression was conducted and observed with a homemade optical setup. During the deformation process, an optical camera equipped with a lens was used to record images. A camera (UI-1220LE-C-HQ, IDS, Germany) equipped with a lens (MRD07420, Nikon, Japan) of 40x magnification was used for side views and a microscope (LV-UEP, Nikon, Japan) equipped with a lens (566039,

Leica, Germany) of 20× magnification was used for top views. Before the deformation process, sample and indenter were set in focus simultaneously by adjusting the base, and then the indenter was moved exactly to the top of the sample by applying the displacement load step by step. The change in the force sensor response during loading was monitored. Once the remarkable response change of the force sensor occurred, the motion of the indenter was immediately stopped. At that time, the indenter was exactly on top of the sample.

Statistical Analysis: No pre-processing of data was performed. Data in Figure 4a are presented as mean ± standard deviation (SD). The sample size for each statistical analysis was 90. The software used for statistical analysis was Origin.

Supporting Information

Supporting Information is available from the Wiley Online Library or from the author.

Acknowledgements

This work was supported by the EIPHI Graduate School [grant number ANR-17-EURE-0002], the French Investissements d'Avenir program, project ISITEBFC [grant number ANR-15-IDEX-03], the National Natural Science Foundation of China [grant numbers 11972008], and the China Scholarship Council. This work was also supported by the french RENATECH network and its FEMTO-ST technological facility.

Conflict of Interest

The authors declare no conflict of interest.

Data Availability Statement

The data that support the findings of this study are available from the corresponding author upon reasonable request.

Keywords

3D micro-structuration, chiral metamaterials, clutch, friction, micro-stepper engines

Received: May 4, 2022

Revised: May 21, 2022

Published online:

- [1] H. W. Dickinson, *A short history of the steam engine*, Cambridge University Press **2011**.
- [2] F. Fraternali, N. Singh, A. Amendola, G. Benzoni, G. W. Milton, *Nonlinear Dyn.* **2021**, *106*, 3147.
- [3] R. Fleury, D. L. Sounas, A. Alú, *Nat. Commun.* **2015**, *6*, 5905.
- [4] Y. Cao, M. Derakhshani, Y. Fang, G. Huang, C. Cao, *Advanced Functional Materials* **2021**.
- [5] S. K. Karan, R. Bera, S. Paria, A. K. Das, S. Maiti, A. Maitra, B. B. Khatua, *Adv. Energy Mater.* **2016**, *6*, 1601016.
- [6] U. Kiencke, L. Nielsen, *Automotive control systems: for engine, drive-line, and vehicle* **2000**.
- [7] A.-I. Bunea, D. Martella, S. Nocentini, C. Parmeggiani, R. Taboryski, D. S. Wiersma, *Advanced Intelligent Systems* **2021**, *3*, 2000256.
- [8] G. W. Milton, *The Theory of Composites*, Cambridge University Press, Cambridge, UK **2002**.
- [9] W. C. Orthwein, *Clutches and brakes: design and selection*, CRC Press **2004**.
- [10] C. C. Alcântara, F. C. Landers, S. Kim, C. De Marco, D. Ahmed, B. J. Nelson, S. Pané, *Nature communications* **2020**, *11*, 1.
- [11] K. Melde, E. Choi, Z. Wu, S. Palagi, T. Qiu, P. Fischer, *Adv. Mater.* **2018**, *30*, 1704507.
- [12] V. Magdanz, S. Sanchez, O. G. Schmidt, *Adv. Mater.* **2013**, *25*, 6581.
- [13] H. Zhang, Z. Li, C. Gao, X. Fan, Y. Pang, T. Li, Z. Wu, H. Xie, Q. He, *Sci. Robot.* **2021**, *6*, 9519eaaz.
- [14] S. Tottori, L. Zhang, F. Qiu, K. K. Krawczyk, A. Franco-Obregón, B. J. Nelson, *Advanced materials* **2012**, *24*, 811.
- [15] A. Münchinger, V. Hahn, D. Beutel, S. Woska, J. Monti, C. Rockstuhl, E. Blasco, M. Wegener, *Advanced Materials Technologies* **2021**, 2100944.
- [16] E. Avci, M. Grammatikopoulou, G.-Z. Yang, *Adv. Opt. Mater.* **2017**, *5*, 1700031.
- [17] Q. Ji, J. Moughames, X. Chen, G. Fang, J. J. Huaroto, V. Laude, J. A. I. Martínez, G. Ulliac, C. Clévy, P. Lutz, et al., *Communications Materials* **2021**, *2*, 1.
- [18] V. Hahn, P. Kiefer, T. Frenzel, J. Qu, E. Blasco, C. Barner-Kowollik, M. Wegener, *Adv. Funct. Mater.* **2020**, *30*, 1907795.
- [19] L. Dai, D. Lin, X. Wang, N. Jiao, L. Liu, *ACS Appl. Mater. Interfaces* **2020**, *12*, 57587.
- [20] A. S. Gladman, E. A. Matsumoto, R. G. Nuzzo, L. Mahadevan, J. A. Lewis, *Nat. Mater.* **2016**, *15*, 413.
- [21] D. Gräfe, M. Gernhardt, J. Ren, E. Blasco, M. Wegener, M. A. Woodruff, C. Barner-Kowollik, *Adv. Funct. Mater.* **2021**, *31*, 2006998.
- [22] H. A. Houck, P. Müller, M. Wegener, C. Barner-Kowollik, F. E. Du Prez, E. Blasco, *Adv. Mater.* **2020**, *32*, 2003060.
- [23] A. Paolini, S. Kollmannsberger, E. Rank, *Addit. Manuf.* **2019**, *30*, 100894.
- [24] M. Kadic, G. M. Milton, M. van Hecke, M. Wegener, *Nat. Rev. Phys.* **2019**, *1*, 198.
- [25] C. Kern, G. W. Milton, M. Kadic, M. Wegener, *New J. Phys.* **2018**, *20*, 083034.
- [26] V. Hahn, T. Messer, N. M. Bojanowski, E. R. Curticean, I. Wacker, R. R. Schröder, E. Blasco, M. Wegener, *Nat. Photonics* **2021**, *15*, 932.
- [27] X. Chen, J. Moughames, Q. Ji, J. A. I. Martínez, H. Tan, S. Adrar, N. Laforge, J.-M. Cote, S. Euphrasie, G. Ulliac, et al., *Extreme Mechanics Letters* **2020**, *41*, 101048.
- [28] T. Bückmann, R. Schittny, M. Thiel, M. Kadic, G. W. Milton, M. Wegener, *New journal of physics* **2014**, *16*, 033032.
- [29] A. Bossart, D. M. Dykstra, J. van der Laan, C. Coulais, *Proc. Natl. Acad. Sci. USA* **2021**, *118*, 21.
- [30] K. E. Evans, A. Alderson, *Adv. Mater.* **2000**, *12*, 617.
- [31] B. Florijn, C. Coulais, M. van Hecke, *Phys. Rev. Lett.* **2014**, *113*, 175503.
- [32] M. Brandenbourger, X. Locsin, E. Lerner, C. Coulais, *Nature communications* **2019**, *10*, 1.
- [33] R. Fleury, D. L. Sounas, C. F. Fleck, M. R. Haberman, A. Alú, *Science* **2014**, *343*, 516.
- [34] G. W. Milton, *J. Mech. Phys.* **2013**, *61*, 1543.
- [35] J. T. B. Overvelde, J. C. Weaver, C. Hoberman, K. Bertoldi, *Nature* **2017**, *541*, 347.
- [36] H. Nassar, B. Yousefzadeh, R. Fleury, M. Ruzzene, A. Alú, C. Daraio, A. N. Norris, G. Huang, M. R. Haberman, *Nat. Rev. Mater.* **2020**, *5*, 667.
- [37] C. Coulais, E. Teomy, K. De Reus, Y. Shokef, M. Van Hecke, *Nature* **2016**, *535*, 529.
- [38] T. A. M. Hewage, K. L. Alderson, A. Alderson, F. Scarpa, *Adv. Mater.* **2016**, *28*, 10323.

- [39] H. M. A. Kolken, S. Janbaz, S. M. A. Leeflang, K. Lietaert, H. H. Weinans, A. A. Zadpoor, *Mater. Horiz.* **2018**, *5*, 28.
- [40] C. Coulais, A. Sabbadini, F. Vink, M. van Hecke, *Nature* **2018**, *561*, 512.
- [41] R. M. Neville, F. Scarpa, A. Pirrera, *Sci. Rep.* **2016**, *6*, 31067.
- [42] F. Wenz, I. Schmidt, A. Lechner, T. Lichti, S. Baumann, H. Andrae, C. Eberl, *Adv. Mater.* **2021**, *33*, 2008617.
- [43] Y. Zhu, M. Birla, K. R. Oldham, E. T. Filipov, *Adv. Funct. Mater.* **2020**, *30*, 2003741.
- [44] M. J. Mirzaali, S. Janbaz, M. Strano, L. Vergani, A. A. Zadpoor, *Sci. Rep.* **2018**, *8*, 965.
- [45] Chen , Tian, Bilal, R. Osama, Shea , Kristina, Daraio , Chiara, *Proc. Natl. Acad. Sci. USA* **2018**, *115*, 5698.
- [46] S. Janbaz, F. Bobbert, M. Mirzaali, A. Zadpoor, *Mater. Horiz.* **2019**, *6*, 1138.
- [47] B. Florijn, C. Coulais, M. van Hecke, *Soft Matter* **2016**, *12*, 8736.
- [48] C. Coulais, D. Sounas, A. Alù, *Nature* **2017**, *542*, 461.
- [49] J. Moughames, X. Porte, M. Thiel, G. Ulliac, L. Larger, M. Jacquot, M. Kadic, D. Brunner, *Optica* **2020**, *7*, 640.
- [50] J. Moughames, X. Porte, L. Larger, M. Jacquot, M. Kadic, D. Brunner, *Opt. Mater. Express* **2020**, *10*, 2952.
- [51] T. Frenzel, M. Kadic, M. Wegener, *Science* **2017**, *358*, 1072.
- [52] C. Yang, K. Yang, Y. Tian, M. Fu, L. Hu, *Extreme Mechanics Letters* **2021**.
- [53] R. Zhong, X. Chen, B. Zheng, M. Fu, L. Hu, *Compos. Struct.* **2019**, *226*, 111232.
- [54] L. R. Long, M. H. Fu, L. L. Hu, *Composite Structures* **2020**, 113429.
- [55] S. Xia, L. Ponson, G. Ravichandran, K. Bhattacharya, *Phys. Rev. Lett.* **2012**, *108*, 19.
- [56] N. R. Brodnik, S. Brach, C. M. Long, G. Ravichandran, K. Bhattacharya, *Phys. Rev. Lett.* **2021**, *21*, 025503.
- [57] Y. Chen, T. Frenzel, S. Guenneau, M. Kadic, M. Wegener, *J. Mech. Phys. Solids* **2020**, *137*, 103877.